Three-dimensional instantaneous mantle flow induced by subduction

C. Piromallo,[1] T. W. Becker,[2] F. Funiciello,[3] and C. Faccenna[3]

Received 2 December 2005; revised 16 February 2006; accepted 16 March 2006; published 19 April 2006.

[1] We conduct three-dimensional subduction experiments by a finite element approach to study flow around slabs, which are prescribed based on a transient stage of upper mantle subduction from a laboratory model. Instantaneous velocity field solutions are examined, focusing on the toroidal *vs*. poloidal components as a function of boundary conditions, plate width, and viscosity contrast between slab and mantle. We show how the slab-to-mantle viscosity ratio determines the strength of toroidal flow, and find that the toroidal flow component peaks for slab/mantle viscosity ratios ~100, independent of slab width or geometry. **Citation:** Piromallo, C., T. W. Becker, F. Funiciello, and C. Faccenna (2006), Three-dimensional instantaneous mantle flow induced by subduction, *Geophys. Res. Lett.*, *33*, L08304, doi:10.1029/2005GL025390.

1. Introduction

[2] Insight into subduction and related mantle circulation has been gained by comparison of natural observables with predictions from analytical, numerical and laboratory models. Using two-dimensional (2-D) models, corner flow theory [e.g., *Tovish et al.*, 1978] evolved into models that explore, for example, the sensitivity of subduction and induced mantle flow to trench migration [e.g., *Garfunkel et al.*, 1986; *Zhong and Gurnis*, 1996; *Christensen*, 1996; *Kincaid and Sacks*, 1997; *Enns et al.*, 2005]. However, seismic anisotropy studies indicate that moving trench systems are complex three-dimensional (3-D) environments [e.g., *Smith et al.*, 2001], where a simple 2-D approximation fails. Full 3-D modelling is computationally challenging, and even inherently 3-D laboratory models have long been intentionally constrained to quasi 2-D [e.g., *Kincaid and Sacks*, 1997; *Guillou-Frottier et al.*, 1995]. More recent laboratory models allow for fully 3-D, kinematically prescribed [*Buttles and Olson*, 1998; *Kincaid and Griffiths*, 2003, 2004], or dynamically self-consistent [*Funiciello et al.*, 2003, 2004a, 2006; *Schellart*, 2004] trench migration, representing a significant advance for a comprehensive study of mantle circulation. These works highlight the importance of the toroidal *vs.* poloidal mantle flow components during trench migration, but the intrinsic experimental limitations of a laboratory model restrict quantitative analysis.

[3] Thus, we model the 3-D instantaneous mantle velocity field induced by a free slab using the finite element approach of *Moresi and Solomatov* [1995] and *Zhong et al.* [2000] and a prescribed slab density and shape based on an intermediate stage of a laboratory subduction model [*Funiciello et al.*, 2006]. Numerical modelling of 3-D flow has previously addressed several related issues, including the effect on geoid anomalies of lateral strength variation of slabs [*Moresi and Gurnis*, 1996] and plates [*Zhong and Davies*, 1999]; the role of faults, rheology and viscosity for plate generation [*Zhong et al.*, 1998]; and the effects of lateral variations in viscosity on deformation and flow in subduction zones [*Billen et al.*, 2003; *Funiciello et al.*, 2004b; *Stegman et al.*, 2006]. Here we focus on the instantaneous mantle flow induced by subduction, and explore the flow pattern of a 3-D versus a 2-D setting, the role of boundary conditions, plate width, and viscosity contrasts between slab and mantle.

2. Numerical Method and Model Set Up

[4] The convection problem is solved using a regional version, *regcitcom*, of the 3-D finite element code *CitcomS* [*Moresi and Solomatov*, 1995; *Zhong et al.*, 2000; *Tan et al.*, 2002]. *CitcomS* solves the conservation equations for mass, momentum and energy in the Boussinesq approximation, assuming that the mantle is an incompressible viscous medium (see *Zhong et al.* [2000] for details). A slab shape with constant temperature contrast is assigned from a transient stage of a reference laboratory model [*Funiciello et al.*, 2006], in which the slab tip reaches ~half the box depth. The numerical domain reproduces the one adopted in the laboratory model and is $7.4 \times 7.4 \times 1$ in x, y, z directions respectively, representing a box that is ~4900 km wide and 660 km deep (one non-dimensional length unit scales to 660 km). The slab thickness is 0.15, corresponding to ~100 km. Resolution is 384×384 elements in the horizontal and 48 in the vertical direction; convergence of the numerical solution was tested by doubling the resolution, and velocity variations were less than 5%. We assign a constant density contrast to the slab which scales absolute velocities along with the background viscosity akin to a Stokes' sinker. All viscosities are Newtonian and constant within the slab and mantle; slab viscosities are chosen as 1, 10, 50, 10^2, $5{\cdot}10^2$, 10^3, and 10^4 times the mantle viscosity. In nature, power-law rheologies and lateral viscosity contrasts will clearly change the details of mantle flow [e.g., *Billen and Hirth*, 2005] but we expect the general insights into the dominant controls on the velocity field to remain valid. We study the instantaneous flow field solution for models with free- and no-slip boundary conditions (BCs) at lateral and bottom sides (the surface is always free-slip), to explore both end-member cases and to be able to compare with the laboratory setup, which is no-slip.

3. 2-D Versus 3-D

[5] We show here results for models with a viscosity contrast of $\eta' = 10^4$ between slab and mantle, directly

[1]Istituto Nazionale di Geofisica e Vulcanologia, Rome, Italy.
[2]Department of Earth Sciences, University of Southern California, Los Angeles, California, USA.
[3]Dipartimento di Scienze Geologiche, Università degli Studi "Roma Tre," Rome, Italy.

0094-8276/06/2005GL025390$05.00

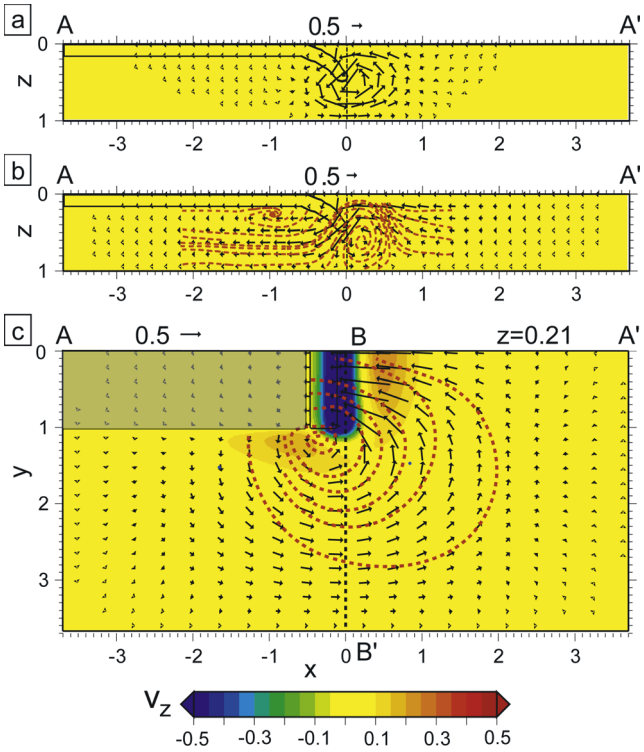

Figure 1. Velocity field for models with $\eta' = 10^4$, slab width $w = 1.85$, no-slip BCs at lateral and bottom sides, free-slip at surface. Lengths are normalized to the box depth. Side view on a vertical plane through the slab centerline in the (a) 2-D and (b) 3-D case. Arrows are velocity vectors projected onto the x-z plane. (c) Map view (3-D case) on a horizontal plane at sub-lithospheric depth $z = 0.21$ (∼1.5 times the slab thickness). Only half box is shown, given the mirror symmetry of models along the mid-plane perpendicular to the trench. Grey-shaded rectangle is the plate at the surface, outlined rectangle is the slab intersection with the plane at $z = 0.21$. Arrows are velocity vectors projected onto the x-y plane, color plot gives the magnitude of the vertical velocity component. Arrows in the vertical plane are reduced by a factor of two with respect to those in the horizontal plane for plotting reasons. Non-dimensional velocities need to be multiplied by a factor of ∼0.17 cm/yr to get the corresponding values in nature, assuming 10^{21} Pa·s as reference viscosity. Streamlines of the corresponding laboratory model [*Funiciello et al.*, 2006] are represented on both side and map views as dashed lines.

comparable to the parameters of the laboratory models. We approximate the 2-D setting by a slab extending laterally for the whole box width. In 2-D (Figure 1a) the flow is clearly confined in the vertical plane where we observe the characteristic subduction velocity pattern [cf. *Garfunkel et al.*, 1986]; for retrograde slab migration, a poloidal cell of return flow exists beneath the slab tip. ''Trench suction'' is responsible for back-arc motion toward trench, thus generating extension in the back-arc region, then upward flow in front of the slab.

[6] In Figures 1b–1c we show a 3-D model with slab width $w = 1.85$ (i.e., 0.25 the box width). Return flow in the vertical plane along the slab centerline is again observed, though characterized by less vigorous circulation under the slab tip (Figure 1b) compared to the 2-D case (Figure 1a); the return flow (v_x component) below the tip is reduced by ∼75%. This is due to the fact that mantle material is now allowed to move around the slab lateral edges, in response to both verticalization and roll-back of the free slab in this transient stage, as also observed in laboratory models [e.g., *Kincaid and Griffiths*, 2003; *Funiciello et al.*, 2006]. On a horizontal plane at sub-lithospheric depth (Figure 1c), the toroidal flow component describes symmetrical cells at the slab edges. In addition, we observe positive vertical velocities (red-upward directed) not only in front of the slab but also close to its lateral edges, due to the extrusion of mantle material from below the inclined slab.

[7] Overall, velocity patterns match those of the corresponding laboratory models [*Funiciello et al.*, 2006], whose streamlines are superimposed on the velocity fields of Figures 1b–1c for an initial, qualitative comparison. Note the good match of the return flow cell below the slab tip and around its lateral edge, as well as the uplifted streamlines in the wedge. Discrepancies are likely due to surface boundary conditions, which are free surface in the laboratory and free-slip in the numerical models; they may also be caused by methodological difficulties in determining the velocity field, such as in the case of the vortex underneath the slab. We consider the match between lab and numerics encouraging and leave quantitative comparisons for a future study.

4. Role of Plate Width

[8] Figure 2 shows profiles of horizontal velocities v_x across the slab (profile BB′ on Figure 1c) for different slab width w ($1/16 < w < 1/3$ of the box width) and BCs, summarizing the characteristics of the horizontal return flow in terms of geometry. In front of the slab ($y' < 0$, where $y' = y - w/2$) v_x increases with w up to w∼1 and then decreases for larger slab widths. This is also the case for maximum vertical velocities (not shown here), indicating that in this area velocity is controlled by the box-height in the transient stage. Outside the slab ($y' > 0$) v_x increases with w showing that larger slabs trigger faster horizontal return flows. The characteristic length-scale associated with this arctan-like

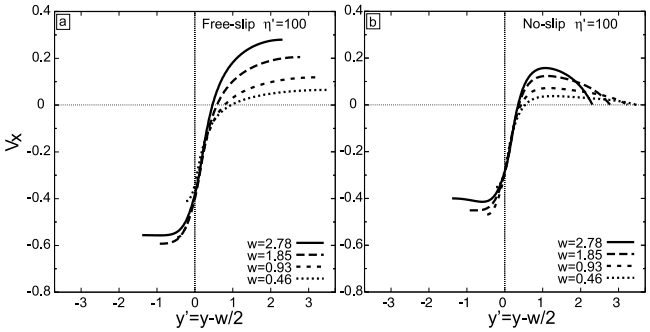

Figure 2. Velocity component v_x along profile BB′, parallel to y-axis and centred at $x = 0$, through the horizontal layer of Figure 1c. Curves are related to models with $\eta' = 10^2$ and different w, (a) with free-slip and (b) no-slip BCs. The y-coordinate is shifted by the slab half-width ($y' = y - w/2$) to ease comparison of different models. Non-dimensional velocities need to be multiplied by a factor of ∼4.22 cm/yr to get the corresponding values in nature, with 10^{21} Pa·s as reference viscosity.

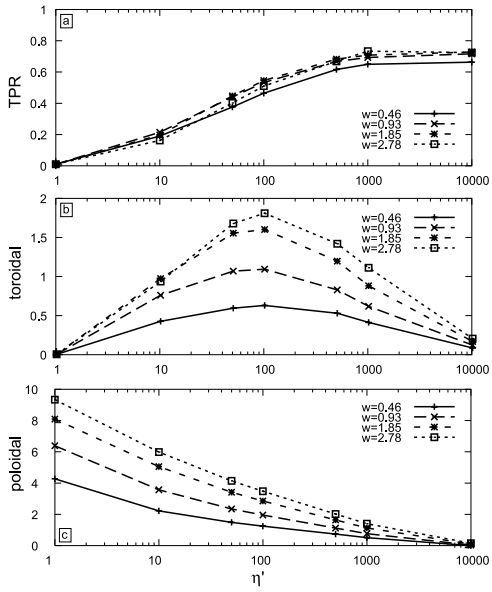

Figure 3. (a) Total toroidal/poloidal ratio (*TPR*), (b) toroidal and (c) poloidal components computed following *Tackley* [2000] as a function of η' (see text for details). Each curve is related to a slab of different *w*. Free-slip BC at side and bottom boundaries.

velocity increase is ~1/3 the box height for all free-slip cases.

[9] No-slip BCs have an overall damping effect on the velocity, as expected (Figure 2b). The return flow transition-length, where $v_x = 0$ and flow changes opposite direction, depends on *w*. Moreover, the return flow is more confined to the slab edge compared to the free-slip case.

5. Role of Viscosity Contrast

[10] For no lateral viscosity variations, the slab induced flow is similar to that of a Stokes' sinker; increasing η' causes the mantle to flow around slab edges with a toroidal pattern on a horizontal plane (Figure 1c). On a vertical plane through the slab centerline we also observe a dominant component in the negative *x*-axis direction (Figure 1b), which fades away when decreasing the viscosity contrast η'. We decompose velocities into toroidal and poloidal components [e.g., *Bercovici*, 1993] to quantify the flow characteristics. Following *Tackley* [2000], the 2-D velocities on each horizontal layer are expressed as the sum of an irrotational and a divergence-free field. We solve Poisson's equation for the poloidal and toroidal potentials and set their gradient or value to zero on the boundaries for free- or no-slip cases, respectively. The vertical velocity component v_z is added to the poloidal field. The RMS of poloidal and toroidal velocities, $RMSv_{pol}$ and $RMSv_{tor}$, is computed for each layer and then summed over the layers to give the total toroidal/poloidal ratio (*TPR*) as $TPR = \sum_{i=1}^{N} RMSv_{tor} / \sum_{i=1}^{N} RMSv_{pol}$, where *N* is the number of layers.

[11] Figure 3a shows the *TPR* as a function of η', for free-slip BCs and fixed buoyancy contrast. Note that the *TPR* increases with η', ranging from ~0.2 ($\eta' = 10$) to ~0.7 ($\eta' = 10^4$), nearly independent of *w*. This trend is due to the combined effect of the poloidal and toroidal components as the flow becomes more similar to that of a rigid sinking body. The poloidal component, as well as absolute maximum velocities, decrease monotonically for increasing η' (Figure 3c), because stiffer slabs suffer from more viscous dissipation. The toroidal component instead increases up to $\eta' \sim 10^2$ and decreases for larger contrasts (Figure 3b). This peak in toroidal flow is likely due to the interplay between induced toroidal motion (which becomes significant once viscosity contrasts are larger than ~10) and increased slab bending resistance (which tends to inhibit motions, as also seen for the poloidal component). Although the *TPR* is nearly independent of *w*, wider slabs have larger poloidal and toroidal terms due to their higher negative buoyancy and ability to laterally displace material. No-slip cases show very similar trends, though the maximum *TPR* is reduced to ~40% with respect to 70% for the free-slip case.

[12] To evaluate the role of transients in our models, we conducted similar experiments for a fully developed, steady-state roll-back stage which shows similar, though more vigorous, horizontal flow patterns, again in agreement with *Funiciello et al.* [2006]. While toroidal and poloidal flow are stronger in amplitude for steady-state subduction, the toroidal strength shows a similar peak around $\eta'_{tmax} \sim 10^2$, and the *TPR* as a function of η' is within 10% of that of the transient stage presented here.

6. Discussion and Conclusions

[13] From our 3-D modeling we are able to quantify the importance of the large scale toroidal flow component in the horizontal plane, triggered in the mantle by the motion of a stiff, free slab. Since we focus on a transient subduction stage where the slab tip reaches halfway the box bottom, the flow pattern we observe is the result of both slab verticalization and roll-back motion. The 3-D approach shows that the toroidal flow plays a key role in affecting the circulation geometry in the vertical plane, compared to the 2-D case. In particular, the material resumed at surface in the back-arc wedge by the return flow cell below the slab tip is minimal with respect to 2-D models [*Tovish et al.*, 1978], in agreement with laboratory models [*Funiciello et al.*, 2006]. Furthermore, we find that circulation is characterized by a non-negligible upward flow component close to slab sides (Figure 1c), that could have important implications to interpret local tectonic structure at slab edges.

[14] In our models of a transient subduction stage, the characteristic spatial length-scale influencing the flow pattern is the box height. These models are closed at 660 km, rather than using a deeper box with an increase in viscosity, which might affect the poloidal circulation and characteristic length-scales of the flow. Moreover, we show that BCs, besides the expected effect of damping/enhancing the flow velocities, also influence its pattern. In particular, in proximity of the slab the flow field is similar for no- and free-slip BCs, while strong variations exist elsewhere, as expected for a Stokes problem. Laboratory models can thus be considered a good approximation to numerical models, which are typically free-slip, if we restrict our observations close to the slab. In nature of course neither no-, nor free-slip boundary conditions apply, but the larger scale regional setting has to be considered.

[15] By modelling different viscosity contrasts between slab and mantle, we show that significant return flow around edges can only be obtained for stiff slabs. This is comparable with results by *Kincaid and Griffiths* [2003], who discussed return flow as a function of prescribed trench rollback, for a rigid plate (the end member, $\eta' = \infty$). Here we obtain similar flow patterns for a slab that sinks freely into the mantle. Moreover, we find that the strength of the *TPR* increases with η', nearly independent of slab width. This relationship is affected by the lateral BCs and might be modified for time-dependent subduction, where we expect a more prominent dependence on *w* [*Stegman et al.*, 2006]. We observe that for $\eta' \geq 10^3$ the toroidal flow components make up ~60–70% of the poloidal ones, while we estimate ~40–50% for lower viscosity contrasts ($\eta' \sim 10^2$). We note in our models that the toroidal term peaks for slab/mantle viscosity ratios η'_{tmax} of $\sim 10^2$, independent of slab *w*. This trend is found not only for transient but also for steady-state, rollback subduction. Estimates for effective viscosity contrasts in nature are comparable to, or somewhat higher than η'_{tmax} [*Conrad and Hager*, 1999; *Becker et al.*, 1999]. We suggest that future modelling should explore regional settings where the slab shape can be inferred (e.g., from tomography) and the toroidal flow estimated (e.g., from shear wave splitting), in order to constrain the effective slab/mantle viscosity ratio from the TPR.

[16] Numerical models can be easily quantitatively explored and compared with the velocity field from laboratory models as analyzed by feature tracking [e.g., *Funiciello et al.*, 2006]. Here, our comparison has to remain qualitative, but future efforts will be useful to understand, in particular, the role of mechanical surface boundary conditions for issues such as roll-back.

[17] **Acknowledgments.** We thank all authors that contributed to the development of CitcomS; GeoFramework.org for making the source code available; and B. Kaus, M. Moroni, D. Stegman and an anonymous reviewer for valuable comments. Figure 1 was created using GMT [*Wessel and Smith*, 1998]. Study partly funded by grants MIUR-FIRB RBAU01JMT3 and NSF-EAR0409373. Some of the computation was supported by the University of Southern California Center for High Performance Computing and Communications (www.usc.edu/hpcc).

References

Becker, T. W., C. Faccenna, R. J. O'Connell, and D. Giardini (1999), The development of slabs in the upper mantle: Insights from numerical and laboratory experiments, *J. Geophys. Res.*, *104*, 15,207–15,226.

Bercovici, D. (1993), A simple model of plate generation from mantle flow, *Geophys. J. Int.*, *114*, 635–650.

Billen, M. I., and G. Hirth (2005), Newtonian versus non-Newtonian upper mantle viscosity: Implications for subduction initiation, *Geophys. Res. Lett.*, *32*, L19304, doi:10.1029/2005GL023457.

Billen, M. I., M. Gurnis, and M. Simons (2003), Multiscale dynamics of the Tonga-Kermadec subduction zone, *Geophys. J. Int.*, *153*, 359–388.

Buttles, J., and P. Olson (1998), A laboratory model of subduction zone anisotropy, *Earth Planet. Sci. Lett.*, *164*, 245–262.

Conrad, C. P., and B. Hager (1999), The effects of plate bending and fault strength at subduction zones on plate dynamics, *J. Geophys. Res.*, *104*, 17,551–17,571.

Christensen, U. R. (1996), The influence of trench migration on slab penetration into the lower mantle, *Earth Planet. Sci. Lett.*, *140*, 27–39.

Enns, A., T. W. Becker, and H. Schmeling (2005), The dynamics of subduction and migration for viscosity stratification, *Geophys. J. Int.*, *160*, 761–775.

Funiciello, F., C. Faccenna, D. Giardini, and K. Regenauer-Lieb (2003), Dynamics of retreating slabs: 2. Insights from three-dimensional laboratory experiments, *J. Geophys. Res.*, *108*(B4), 2207, doi:10.1029/2001JB000896.

Funiciello, F., C. Faccenna, and D. Giardini (2004a), Role of lateral mantle flow in the evolution of subduction system: Insights from 3-D laboratory experiments, *Geophys. J. Int.*, *157*, 1393–1406.

Funiciello, F., C. Piromallo, M. Moroni, T. Becker, C. Faccenna, H. A. Bui, and A. Cenedese (2004b), 3-D laboratory and numerical models of mantle flow in subduction zones, *Eos Trans. AGU*, *85*(47), Fall Meet. Suppl., Abstract T21B-0527.

Funiciello, F., M. Moroni, C. Piromallo, C. Faccenna, A. Cenedese, and H. A. Bui (2006), Mapping mantle flow during retreating subduction: Laboratory models analyzed by feature tracking, *J. Geophys. Res.*, *111*, B03402, doi:10.1029/2005JB003792.

Garfunkel, Z., D. L. Anderson, and G. Schubert (1986), Mantle circulation and lateral migration of subducting slabs, *J. Geophys. Res.*, *91*, 7205–7223.

Guillou-Frottier, L., J. Buttles, and P. Olson (1995), Laboratory experiments on structure of subducted lithosphere, *Earth Planet. Sci. Lett.*, *133*, 19–34.

Kincaid, C., and R. W. Griffiths (2003), Laboratory models of the thermal evolution of the mantle during rollback subduction, *Nature*, *425*, 58–62.

Kincaid, C., and R. W. Griffiths (2004), Variability in flow and temperatures within mantle subduction zones, *Geochem. Geophys. Geosyst.*, *5*, Q06002, doi:10.1029/2003GC000666.

Kincaid, C., and I. S. Sacks (1997), Thermal and dynamical evolution of the upper mantle in subduction zones, *J. Geophys. Res.*, *102*, 12,295–12,315.

Moresi, L., and M. Gurnis (1996), Constraints on the lateral strength of slabs from three-dimensional dynamic flow models, *Earth Planet. Sci. Lett.*, *138*, 15–28.

Moresi, L., and V. S. Solomatov (1995), Numerical investigation of 2D convection with extremely large viscosity variation, *Phys. Fluids*, *7*, 2154–2162.

Schellart, W. P. (2004), Kinematics of subduction and subduction-induced flow in the upper mantle, *J. Geophys. Res.*, *109*, B07401, doi:10.1029/2004JB002970.

Smith, G. P., D. A. Wiens, K. M. Fischer, L. M. Dorman, S. C. Webb, and J. A. Hildebrand (2001), A complex pattern of mantle flow in the Lau backarc, *Science*, *292*, 713–716.

Stegman, D. R., J. Freeman, W. P. Schellart, L. Moresi, and D. A. May (2006), Influence of trench width on subduction hinge retreat rates in 3-D models of slab rollback, *Geochem. Geophys. Geosyst.*, *7*, Q03012, doi:10.1029/2005GC001056.

Tackley, P. J. (2000), Self-consistent generation of tectonic plates in time-dependent, three-dimensional mantle convection simulations, *Geochem. Geophys. Geosyst.*, *1*(8), doi:10.1029/2000GC000036.

Tan, E., M. Gurnis, and L. Han (2002), Slabs in the lower mantle and their modulation of plume formation, *Geochem. Geophys. Geosyst.*, *3*(11), 1067, doi:10.1029/2001GC000238.

Tovish, A., G. Schubert, and B. P. Luyendyk (1978), Mantle flow pressure and the angle of subduction: Non-Newtonian corner flows, *J. Geophys. Res.*, *83*, 5892–5898.

Wessel, P., and W. H. F. Smith (1998), New, improved version of generic mapping tools released, *Eos Trans. AGU*, *79*(47), 579.

Zhong, S., and G. F. Davies (1999), Effects of plate and slab viscosities on the geoid, *Earth Planet. Sci. Lett.*, *170*, 487–496.

Zhong, S., and M. Gurnis (1996), Interaction of weak faults and non-Newtonian rheology produces plate tectonics in a 3D model of mantle flow, *Nature*, *383*, 245–247.

Zhong, S., M. Gurnis, and L. Moresi (1998), Role of faults, nonlinear rheology, and viscosity structure in generating plates from instantaneous mantle flow models, *J. Geophys. Res.*, *103*, 15,255–15,268.

Zhong, S., M. T. Zuber, L. N. Moresi, and M. Gurnis (2000), Role of temperature-dependent viscosity and surface plates in spherical shell models of mantle convection, *J. Geophys. Res.*, *105*, 11,063–11,082.

T. W. Becker, Department of Earth Sciences, University of Southern California, MC0740, Los Angeles, CA 90089-0740, USA.

C. Faccenna and F. Funiciello, Dipartimento di Scienze Geologiche, Università degli Studi "Roma Tre," Largo San Leonardo Murialdo 1, Rome I-00146, Italy.

C. Piromallo, Istituto Nazionale di Geofisica e Vulcanologia, Via di Vigna Murata, 605, I-00143 Rome, Italy. (piromallo@ingv.it)